Charge rearrangement by sprites over a north Texas mesoscale convective system

William W. Hager,[1] Richard G. Sonnenfeld,[2] Wei Feng,[1] Takeshi Kanmae,[3] H. C. Stenbaek-Nielsen,[3] Matthew G. McHarg,[4] Ryan K. Haaland,[5] Steven A. Cummer,[6] Gaopeng Lu,[6] and Jeff L. Lapierre[2]

Received 18 June 2012; revised 28 September 2012; accepted 3 October 2012; published 16 November 2012.

[1] Charge rearrangement by sprites is analyzed for a mesoscale convective system (MCS) situated in north Texas and east New Mexico on 15 July 2010. During the thunderstorm, electric field data were recorded by the Langmuir Electric Field Array (LEFA), while magnetic field data were recorded by the charge-moment network near Duke University. A high speed (12500 fps) video system operated at Langmuir Laboratory recorded telescopic images of the sprites. Data from the National Lightning Detection Network (NLDN) show that each sprite was preceded by a series of cloud discharges and cloud-to-ground discharges. The triggering event preceding the sprite was typically a positive cloud-to-ground (+CG) stroke. For one out of the 10 sprites that were recorded, there was a positive hump in the electric field a few milliseconds after the +CG return stroke. The size and shape of the hump roughly matched the light intensity emitted from the sprite. The electric field hump is fit by a sprite current that originates in the ionosphere and propagates downward, producing the same effect as a downward moving positive current. The integral under the current hump was 23.9 C when the velocity of the current pulse was between 0.25 c and 0.55 c. The large sprite current was followed by impulsive electromagnetic radiation which has not been previously reported and could be a recoil effect similar to what is called a "K-change" when it is observed in a lightning flash.

Citation: Hager, W. W., R. G. Sonnenfeld, W. Feng, T. Kanmae, H. C. Stenbaek-Nielsen, M. G. McHarg, R. K. Haaland, S. A. Cummer, G. Lu, and J. L. Lapierre (2012), Charge rearrangement by sprites over a north Texas mesoscale convective system, *J. Geophys. Res.*, *117*, D22101, doi:10.1029/2012JD018309.

1. Introduction

[2] This paper studies charge rearrangement in association with sprites, luminous glows in the mesosphere above thunderclouds often extending from about 50 to 90 km in altitude. The video record of a sprite was first obtained in 1989 by *Franz et al.* [1990], while *Sentman et al.* [1995] obtained color imagery of sprites from jet aircraft in the Sprites94 campaign. In the same year, *Boccippio et al.* [1995] obtained visual documentation of sprites from the Yucca Ridge Field Station near Fort Collins, Colorado. Theories for the initiation of sprites include the conventional breakdown theory of *Pasko et al.* [1997] and a runaway breakdown model [e.g., see *Bell et al.*, 1995; *Roussel-Dupré and Gurevich*, 1996]. It was soon recognized [*Boccippio et al.*, 1995] that sprites were often preceded by large, positive cloud-to-ground lightning strokes (+CGs). Previously, current and charge transport in sprites has been analyzed by extracting a low frequency sferic waveform from distant magnetic field measurements, and then using a deconvolution method to estimate the current and charge moment associated with the sprite. These techniques are described in detail by *Cummer and Inan* [2000], while application of these techniques can be found in many papers including those of *Cummer and Inan* [1997], *Cummer et al.* [1998], and *Cummer and Stanley* [1999]. It has often been predicted that the +CG preceding a sprite transferred large amounts of charge. Estimates have ranged from 410 C to 1500 C for daytime sprites [*Stanley et al.*, 2000] to between 50 C and 500 C for nighttime sprites [*Cummer and Inan*, 1997]. In this paper, we analyze where charge is moved by the sprite itself using data from the Langmuir Electric Field Array (LEFA) for sprites associated with lightning strokes located within 500 km of LEFA.

[3] The paper is organized as follows. In section 2 we give an overview of the storm. Section 3 documents the instruments employed in the analysis of the storm, while section 4

[1]Department of Mathematics, University of Florida, Gainesville, Florida, USA.
[2]Department of Physics and Langmuir Laboratory, New Mexico Institute of Mining and Technology, Socorro, New Mexico, USA.
[3]Geophysical Institute, University of Alaska Fairbanks, Fairbanks, Alaska, USA.
[4]U.S. Air Force Academy, Colorado Springs, Colorado, USA.
[5]Department of Physics and Engineering, Fort Lewis College, Durango, Colorado, USA.
[6]Department of Electrical and Computer Engineering, Duke University, Durham, North Carolina, USA.

Corresponding author: W. W. Hager, Department of Mathematics, University of Florida, Gainesville, FL 32611, USA. (hager@ufl.edu)

0148-0227/12/2012JD018309

describes the data collected. Section 5 examines the electric field data in more detail and relates them to the light from the sprites. Section 6 summarizes the results given by *Uman et al.* [1975] for the electromagnetic radiation from a vertical antenna on a perfectly conducting ground plane, while section 7 extends the work of *Uman et al.* [1975] to include a second parallel conducting plane corresponding to the ionosphere. In section 8 we examine the relation between charge transport and the resulting electric field change between two perfectly conducting spheres. In section 9, the vertical antenna model is applied to the electric field connected with a sprite in our study. Finally, section 10 presents the final conclusions gleaned from the data and the analysis.

[4] *Polarity Convention*—The sign convention we employ for the electric field is that it points in the direction of the force exerted on a positive test charge. In the atmospheric electricity community, this is referred to as the physics convention. When reporting our measurements of the vertical electric field, positive electric field points away from the surface of the Earth.

2. Overview of Storm

[5] The storm producing the sprites was a mesoscale convective system (MCS) situated between north Texas and east New Mexico on 15 July 2010. The terrain underneath the storm was relatively flat; the ground elevation was roughly 1000 m, except for the most western edge of the storm in New Mexico, where the ground elevation increased to about 1500 m. The MCS moved toward the southeast. The sprites occurred during the mature phase [see *MacGorman and Rust*, 1998, p. 260] of the storm, between about 5:22 UT and 7:06 UT (or between 11:22 PM 14 July and 1:06 AM 15 July New Mexico time). The sprites appeared in two clusters in time and space. The first set of 7 occurred between 5:22 UT and 5:56 UT, roughly 1 sprite every 5 minutes, on the eastern side of the storm. The ground elevation beneath these sprites was about 1100 m. About 45 minutes later, there were 3 more sprites between 6:41 UT and 7:06 UT, to the west of the initial sprites; the ground elevation under these sprites was about 1300 m. Figure 1 shows the NEXRAD level III composite radar reflectivity at 5:40 UT and at 6:53 UT as recorded by the National Weather Service Station KFDX (Cannon Air Force Base, New Mexico, latitude 34.6342°N, longitude 103.6189°W, elevation 1417 m). For an overview of NEXRAD capabilities, see *Crum et al.* [1993], *Crum and Alberty* [1993], *Crum et al.* [1998], and *Klazura and Imy* [1993]. The plots in Figure 1 show the state of the storm corresponding roughly to each cluster of sprites. Superimposed on each plot is the location of the National Lightning Detection Network (NLDN) lightning event, either +CG return stroke or cloud flash as reported by NLDN, that we associate with each sprite. (See *Cummins and Murphy* [2009] for a comprehensive overview of lightning locating systems with a special focus on NLDN.) The location of LEFA instrument number 2, which is used in our analysis, and the location of Langmuir Laboratory where the sprite videos were recorded, are marked on the west side of the figure. The lightning discharges preceding the sprite were located in the trailing stratiform region, near the deep convective region, consistent with Figure 7 in *Boccippio et al.* [1995].

[6] Many NLDN events were reported before each sprite. For illustration, Figure 2 shows the NLDN events that occurred during the 4 seconds that preceded the +CG return stroke associated with the second sprite photographed on 15 July 2010.

3. Description of the Instruments

[7] Sprites were recorded by a video system located at Langmuir Laboratory (latitude 33.9752 N and longitude 107.1807 W) in the Magdalena Mountains of New Mexico, near Socorro, NM. There were two high speed Phantom 7 cameras operating at 12,500 frames per second and a Watec video camera operating at 30 frames per second. The time resolution of the high speed cameras was 80 microseconds. One of the high speed cameras had a narrow field of view (camera 2), while camera 1 had a wider field of view. The light data presented in this paper are from camera 1, which had an 85 mm lens, giving it a field of view of roughly 3.5° by 7.0°. 10 sprites were recorded by the cameras on 15 July 2010.

[8] The charge transport analysis in this paper is based on data from LEFA, a network of field change sensors consisting of nine slow-antenna stations with amplifiers that are low-pass filtered by a single-pole filter with a 24,100 Hz cut-off frequency. The sampling frequency is 50 kHz with a timing accuracy of 20 μs. To ensure LEFA times are accurate to within a sample period, the PPS and Serial-ASCII outputs of a GPS are OR'd together and digitized as a dedicated "timing channel" together with the three electric field channels. Thus the electric field data has timing information embedded in it and, so long as the GPS is working, no errors in network time or computer time can corrupt the timing. In post-processing, the GPS signals are integrated with the data to produce time-stamped files. The inexpensive Garmin GPS-18 we used is accurate to better than a microsecond, but with a sample period of 20 us, we cannot claim an accuracy of better than 20 us.

[9] Slow-antennae measure electric field changes on timescales less than a designed "high-pass" time constant. The time constant of the sensors used here was $(1/2\pi)$ s or roughly 0.1592 s. LEFA is situated northeast of Langmuir laboratory in a region of size 25 km by 15 km. Each station in the network measures in parallel the electric field on three channels with sensitivities varying between 30 mV/m and 1 kV/m on the sensitive channel, between 1 V/m and 30 kV/m on the medium channel, and between 25 V/m and 750 kV/m on the insensitive channel. This broad dynamic range allows the analysis of electric fields for flashes that are both nearby and distant. The broad range is achieved using an innovative electric field sensor design which is comprised of three concentric rings embedded in an inverted salad bowl (see Figure 3a).

[10] A picture of a LEFA station appears in Figure 3b. The station consists of the inverted salad bowl antenna seen on the right and a ground plane constructed from a section of chainlink fencing. The data-acquisition and networking hardware are contained in the white, waterproof box seen in the figure, while the GPS unit sits on top of the box. A photovoltaic collector charges a gel-type marine battery which powers all the instrumentation. The instrument can be remotely triggered, and data are collected via the Langmuir laboratory wireless network. The antenna seen on the left side of the figure provides network connectivity across 15 km hops to the Langmuir mountaintop, and thence to the New Mexico Tech campus. The LEFA station is surrounded

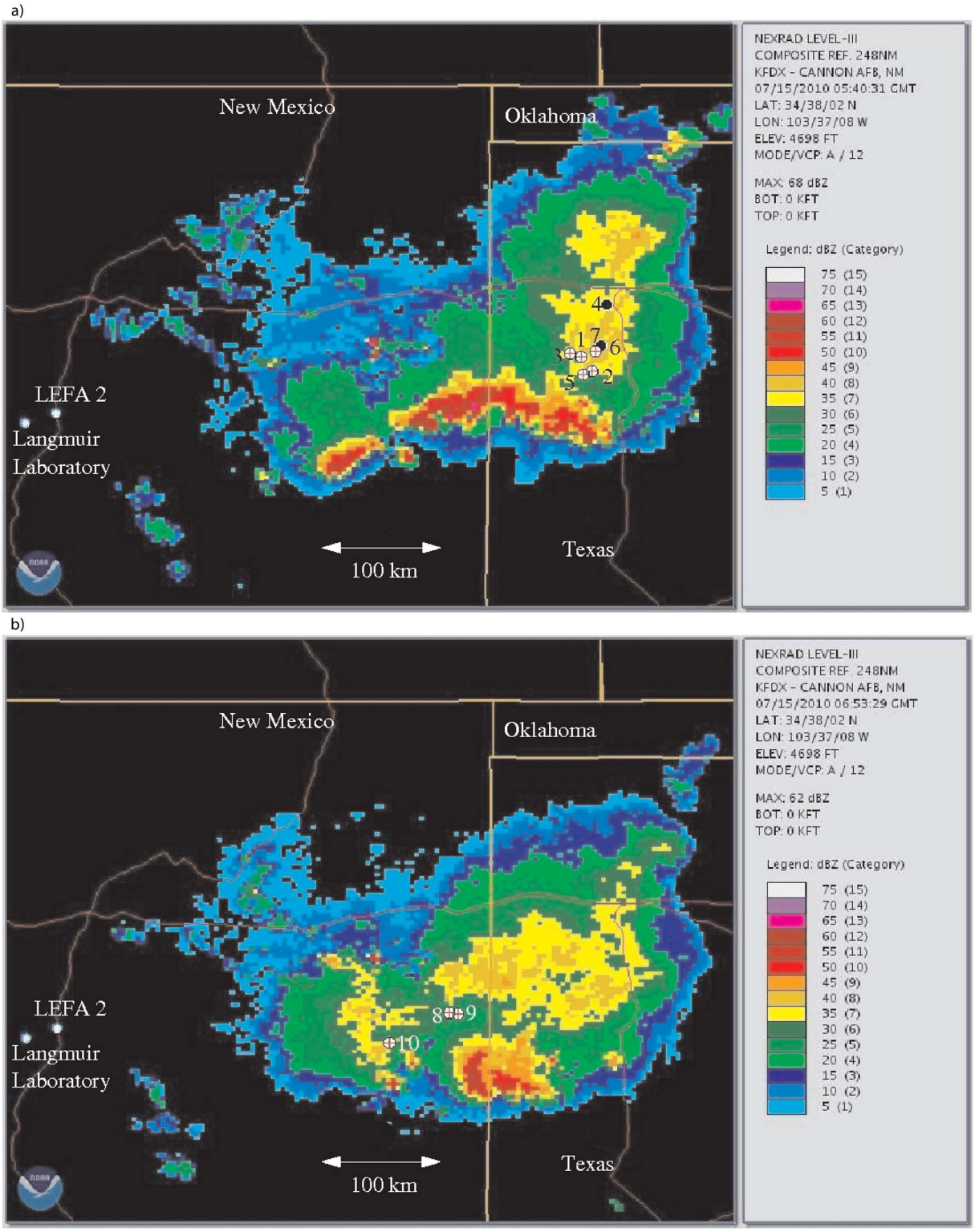

Figure 1. National Weather Service Station KFDX NEXRAD level III composite radar reflectivity on 15 July 2010: (a) at about 5:40 UT and (b) at about 6:53 UT. The location of the National Lightning Detection Network event preceding each sprite is superimposed on the plot. A + sign corresponds to a +CG return stroke, as reported by NLDN, while the black dot corresponds to a cloud flash. The numbers indicate the order in which the sprite occurred, and also correspond to the numbers in Table 2 of this paper. The radar scan extends from eastern New Mexico into northern Texas. The western white dots give the location of LEFA 2 and Langmuir Laboratory where the sprite videos were recorded. LEFA 2 is located on the roof of Workman Center at New Mexico Tech, Socorro, NM.

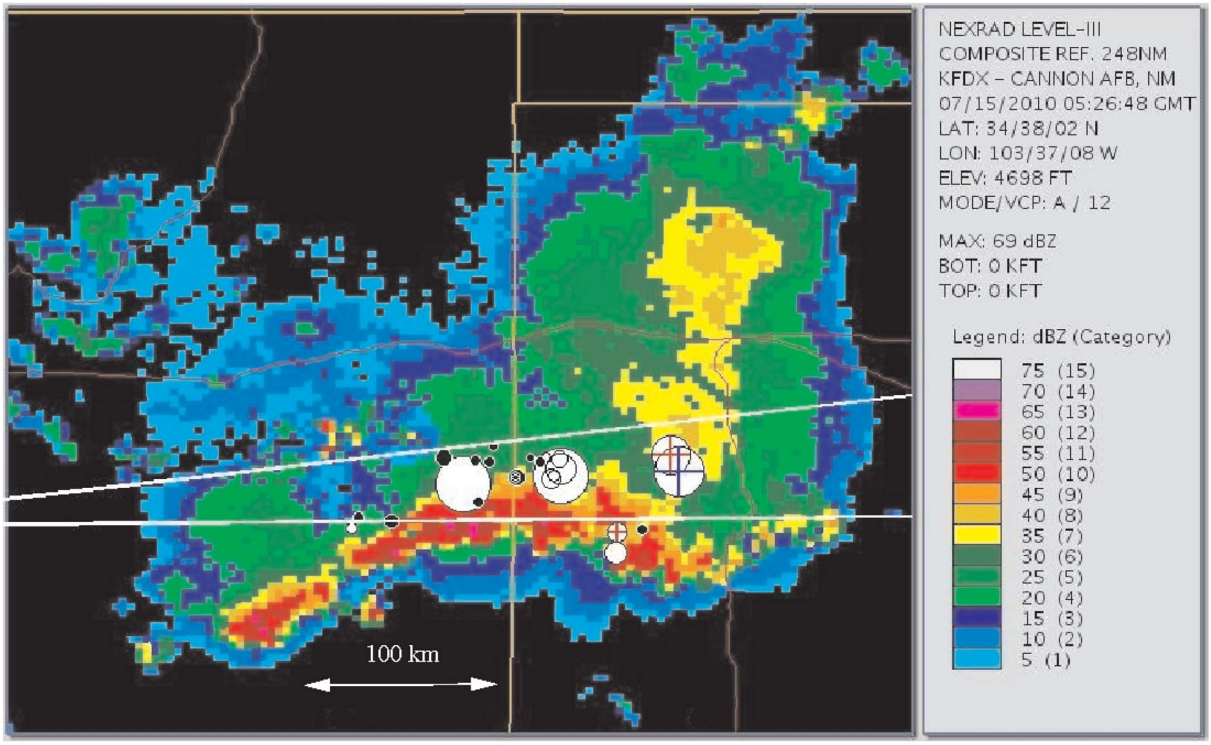

Figure 2. National Weather Service Station KFDX NEXRAD composite reflectivity on 15 July 2010 at about 5:27 UT. Superimposed on the plot are the NLDN locations of the cloud flashes and CG strikes that occurred during the 4 seconds preceding the +CG return stroke associated with sprite 2. Cloud flashes are indicated by black circles, −CGs are indicated by white circles, and +CGs are indicated by + in a white circle. The size of each of these is proportional to the total peak current associated with the flash. For the +CG associated with sprite 2, the + is colored blue. The two white lines show the field of view of the high speed video camera when sprite 2 of Table 2 was photographed. In section 4, Figure 4, we observe that sprite 2, like the associated +CG return stroke, was also roughly centered in the camera's field of view.

by barbed wire to discourage cows and roving animals from eating the GPS unit or disturbing the electronics.

[11] Horizontal magnetic field data were also recorded by Duke's ultra low frequency (ULF) and very low frequency (VLF) instrumentation. The instruments are located in the Duke Forest at latitude 35.970 N and longitude −79.094 E. The frequency range for the ULF system is from 1 to 400 Hz, while the frequency range for the VLF system is from 50 Hz to 30 kHz. The sampling frequency of the ULF system is 2.5 kHz, while the VLF system is 100 kHz. Hence, the timing resolution and accuracy is 400 μs for the ULF system and 10 μs for the VLF system. The noise level of the instruments is about 10 pT RMS.

3.1. LEFA Calibration

[12] The calibration of the LEFA network was performed in the following way. One of the LEFA instruments was operated in the vicinity of Langmuir Laboratory and within 20 m of an E100 field meter described at the following web site: http://www.ee.nmt.edu/langmuir/E100/E100.html. The E100 had been previously calibrated using a flat-plate antenna mounted flush to the ground. Nearby lightning flashes were detected by both the E100 and the LEFA station to obtain an absolute calibration of the LEFA station. The LEFA stations were designed with identical slow-antenna electronics, and component tolerances selected to give an overall gain between instruments that was no more than 0.3%. A test waveform was then applied to a "golden capacitor" in series with the input of the slow-antenna circuit board and it was verified that the output across instruments was indeed equivalent to the 0.3% target.

[13] The precision of the electronics was intended to make cross-calibration unnecessary, but we learned that considerable cross-calibration is necessary to take into account the immediate surroundings of an instrument; the electric field is enhanced by convex topographies (such as mountains or humps) while it is attenuated by concavities (such as valleys or depressions). For example, the instrument at Langmuir Laboratory experienced a much enhanced electric field due to its mountaintop location. In this section, we refer to the instrument at Langmuir Laboratory as the mountain LEFA. Likewise, LEFA 2 on the roof of Workman Center experienced a slightly enhanced electric field due to its location on top of a convex structure. In this section, we refer to the instrument at the Workman Center as the roof LEFA. For the analysis in this paper, we need to know what the instrument would have read if it was situated on a flat plain at its current location. That is,

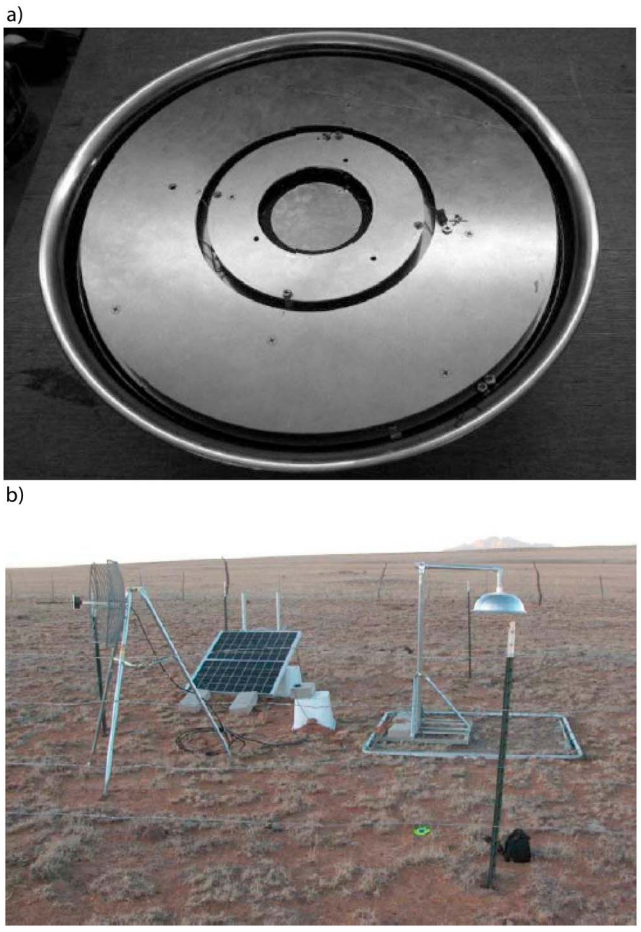

Figure 3. (a) The three ringed sensor developed for LEFA. Each slow antenna plate is attached to a dedicated amplifier. (b) A LEFA station. From right to left, the inverted salad bowl antenna which contains the three ringed sensor shown in Figure 3a, a weather-proof box containing the data-acquisition system and networking hardware, a photovoltaic panel to charge the battery, and an antenna to transmit data to Langmuir Laboratory and then to Workman Center at New Mexico Tech.

we need to remove the local enhancement or attenuation due to the immediate surroundings.

[14] After the instruments were deployed, they were cross calibrated using several hundred distant flashes, ranging from 100 km to 300 km away. The LEFA network spanned 25 km, so as the flash distance crossed 200 km, the response shape to these distant flashes became distance independent, and what remained after the distance dependence was removed was the relative response amplitude. A single measurement is not sufficient to cross-calibrate a slow-antenna, but averaging several hundred flashes allowed us to assign relative responses for each instrument. We found that the amplitude of the distant flash measured by the mountain LEFA was 2.35 times the amplitude of a distant flash seen by LEFA 7 located in the plain. This factor 2.35 was due to the enhancement of the electric field by the mountain. Similarly, the electric field measured by the roof LEFA was enhanced by a factor of 1.31 relative to LEFA 7 due to the effect of building. If the electric field at the roof LEFA from a distant flash was multiplied by the factor 2.35/1.31, we would obtain the electric field expected at the mountain LEFA.

[15] Finally, we perform a numerical computation to relate an electric field at the mountain LEFA to an electric field that would be seen at the location of the roof LEFA if it had been placed on a plain instead of on top of a building. The numerical computation was based on topographic data available from the U.S. Geological Survey on a 10 m grid. Numerically, by placing charges at distant locations (150 km away) around the LEFA network, we could compare the electric field at the mountain LEFA to the electric field at the roof LEFA; in this computation, we only model the surface of the Earth and not the buildings. Numerically, we find that the electric field at the mountain LEFA is enhanced by the factor 2.158 relative to the roof LEFA placed on a flat plain. Hence, by multiplying the measured electric field at the roof LEFA by (2.35/1.31)/2.158, we obtain the value of the electric field at the roof LEFA after removing the effect of the building. The factor 2.35/1.31 transforms the roof electric field to the mountain top electric field, and the factor 1/2.158 converts the mountain top electric field to the electric field on a plain at the location of the roof LEFA. As will be seen in section 5.2.1, the electric fields measured by LEFA are consistent with the magnetic fields measured by the Duke charge-moment array giving further confidence that the calibration process for both LEFA and the Duke instruments was reasonable. The noise on the sensitive channel of LEFA 2, which is used for the plots in this paper, is about 15 mV RMS.

3.2. LEFA Triggering

[16] LEFA is designed to operate more or less continuously. The system starts operation either on operator command (via wireless network) or on a command from a field mill that detects high electric fields. After startup, the entire network streams data continuously to hard drives which are large enough to store more than 5 days of data when the system operates continuously. In actual operation, the drives are large enough to buffer about a month's worth of data, and data can be retrieved over the wireless network at any time. For the data reported in this paper, the instruments were manually enabled for the entire nighttime observing period.

4. Description of the Data Set

[17] During the storm of 15 July 2010, three LEFA stations were operational, stations 2, 5, and 7. Since the MCS was between 300 and 500 km from the LEFA network, only the sensitive channel provided a reliable measurement of the vertical electric field change. Due to the distant location of the storm, all stations detected essentially the same electric field waveshape. In comparing the data records, the amplitude of the noise was smallest for LEFA 2, the instrument located on the roof of Workman Center on the New Mexico Tech campus. Moreover, LEFA 2 was closer to the MCS than the other stations so the amplitude of the electric field at LEFA 2 was slightly larger than the amplitude at the other stations. Hence, our analysis is based on the data obtained from the sensitive channel of LEFA 2.

[18] Ten sprites were recorded by the cameras at Langmuir Laboratory during the storm of 15 July 2010. The azimuth

Table 1. Camera Orientation for Each Sprite During the Storm of 15 July 2010

Sprite Number	Camera Azimuth	Camera Elevation
1	87°	7°
2–8	87°	6°
9	96°	12°
10	93°	12°

and the angle of tilt (elevation) of the cameras during the sprites are given in Table 1. The azimuth is measured relative to true north, and a positive angle is in a clockwise direction. For sprite 1, the elevation was a little too high and much of the sprite was missed. Hence, the tilt was adjusted down for sprites 2 through 8 which were more centered in the high speed camera. Since the camera only caught the right side of sprite 9, the azimuth was reduced for sprite 10; nonetheless, more than 3/4 of this sprite was outside the field of view for the high speed camera.

[19] An overview of the 10 sprites and the associated NLDN data is given in Table 2. The first column describes the predominant structure of the sprite, either carrot, column, or a streamer tip splitting sprite as discussed by *McHarg et al.* [2010]. Sprite 9 was not classified since it appeared in a corner of the field of view. The column labeled delay is the difference between the source time of the sprite (time that the light from the sprite reached the camera minus the transit time for light to travel from the NLDN event to the camera) and the source time of the parent stroke given by NLDN. For brevity, Table 2 does not report the time at which the LEFA stations detected the parent lightning flashes, but in all 10 cases, LEFA timed the onset of the parent flash identically to NLDN within its 20 us timing accuracy, after allowing for the transit time between parent flash and the LEFA stations.

[20] The column labeled light sum gives a measure of the relative intensity of the sprite. It is obtained by adding the light intensity of each pixel in a frame and taking the maximum over all the frames, and then multiplying by 2.5×10^{-13} times the distance (km) from the camera to parent stroke squared. The factor 2.5×10^{-13} is a normalization factor that keeps the light sum between 0 and 100. By multiplying by the distance to the sprite square, it follows that if sprite A is twice the distance from the camera as sprite B, then the light sum for sprite A is multiplied by 4 to account for its greater distance to the camera. In cases where the camera missed much of the sprite, the light sum is not given.

[21] The "Dischgs. before" column in Table 2 gives the number of discharges (return stroke or cloud discharges) that occurred in the region between latitudes 32°N and 35°N and longitudes 101°W and 105°W (which is centered over the storm) in the 3 seconds preceding the NLDN event associated with the sprite. The impulse charge moment change (iCMC) in the last column, as defined by *Cummer and Lyons* [2005], is an estimate of the charge lowered to ground by the lightning flash within 2 ms of the return stroke times the altitude where the charge is removed. This is based on an analysis of the ULF magnetic fields. For sprite 5, the iCMC was too small to estimate; it was less than 50 C km.

[22] NLDN reports two nearly identical positive CGs right before sprites 1 and 2. The time of the two events differs by less than 10 microseconds, the locations differ by at most 1 km, and the peak currents differ by 4%. The interpretation of this event pair, as explained by Kenneth Cummins (private communication, 2011), is that the NLDN found two different self-consistent sets of sensors for the same event and reported both possibilities. In Table 2, we use the location of the return strokes associated with sprites 1 and 2 for which the NLDN reported normalized chi-squared value is smallest. Smaller chi-squared values correspond to better fits to the model. For sprite 2, the chi-squared values for the

Table 2. A Summary of the Video Records (left) and Closely Correlated NLDN Stroke Records (right) for the Sprites Observed in the North Texas MCS on 15 July 2010[a]

	Camera				NLDN							Duke
	Sprite Type	Time (UT)	Delay (ms)	Light Sum	Cur. (kA)	Time (s)	Trigger Type	Lat	Lon	Dist. (km)	Dischgs. Before	iCMC (C km)
1.	Carrot	05:22:01.713809	2.12	??	68	01.710146	+CG	34.3355	−102.2054	460	31	348
2.	Carrot	05:27:09.696409	0.77	90.47	85	09.694066	+CG	34.2303	−102.1123	467	32	610
3.	Carrot	05:32:57.582169	16.34	2.47	33	57.564323	+CG	34.3625	−102.3073	450	35	118
4.	Carrot	05:37:59.544329	3.31	4.81	54	59.539386	IC	34.7223	−101.9781	485	47	207
5.	Carrot	05:45:14.494889	66.62	1.56	22	14.426730	+CG	34.2059	−102.1926	460	31	??
6.	Carrot	05:50:01.584729	13.99	3.08	31	01.569140	IC	34.4187	−102.0331	476	18	100
7.	Column	05:55:54.811609	2.74	2.24	52	54.807285	+CG	34.3785	−102.0794	471	18	226
8.	Column	06:41:36.083769	1.00	0.32	79	36.081595	+CG	34.0208	−103.3953	349	17	356
9.	??	07:00:31.846329	0.37	??	40	31.844769	+CG	34.0088	−103.3247	355	18	408
10.	Split	07:06:09.809929	0.05	??	112	09.808870	+CG	33.7988	−103.9306	301	20	718

[a]In the time column on the right, we do not repeat the hours and seconds which appear on the left. The column labeled delay is an estimate of the time between the initiation of the sprite and the preceding return stroke. The column labeled light sum is a measure of the intensity of the sprite. In each frame, we sum the pixel intensity and then take the maximum over all the frames of the sprite; this maximum is further adjusted to account for the distance to the sprite. The column labeled Duke iCMC (impulse charge moment change) gives the estimated charge moment change occurring within 2 ms of the impulsive event that precedes the sprite. The impulse charge moment change is based on an analysis of the ULF magnetic field data following the return stroke. An entry in the table is given as ?? if there is not enough information to estimate the entry; either the camera missed a significant portion of the sprite or the charge impulse was too small to estimate CMC. In the column labeled trigger type, +CG denotes an NLDN reported positive cloud-to-ground stroke and IC denotes an NLDN cloud discharge. The distance column gives the distance between Langmuir Laboratory and the location of the flash associated with the sprite. The "Dischgs. Before" column gives the total number of ICs plus the numbers of strokes in CGs that occur in the 3 second interval preceding the discharge event associated with the sprite. Figure 2 shows the discharges that precede sprite 2.

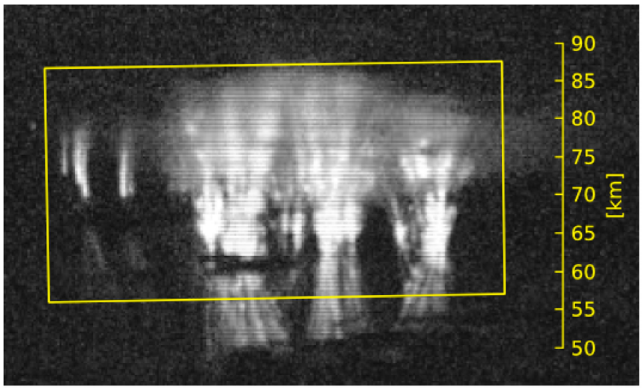

Figure 4. The sprite of 05:27:09 UT as seen by the Watec camera. The sprite extends between 50 and 90 km in altitude. The rectangle shows the field of view of the high speed camera.

NLDN reported events were 0.5 and 2.3 so Table 2 reports the NLDN event corresponding the chi-squared value 0.5. For sprite 1, the chi-squared values were 2.1 and 4.9 so the event corresponding to 2.1 was reported in Table 2.

[23] Columns 9 and 10 of the table give the lat/lon of the putative "parent" CG for each sprite. These coordinates are entirely consistent with the lat/lon derived from the camera orientations described in Table 1. Recall that Figure 1 shows explicitly the camera field-of-view superposed on the NLDN and radar data for sprite #2. An annotated frame of the sprite 2 Watec video appears in Figure 4. The box shows the field of view of the high speed camera. A slow motion movie of sprite 2 is seen at www.math.ufl.edu/~hager/papers/Lightning.

5. Electromagnetic Field Data and Light Intensity

5.1. Return Stroke Without Special Sprite Features

[24] Figure 5 shows electric field radiated by the +CG return stroke for sprite 10, the sprite that was closest to LEFA 2 and which had the largest peak current (112 kA) in the return stroke and the largest impulse charge moment change (718 C km). The zero of the time axis is set at the time of the return stroke as reported by NLDN. LEFA reports its local time; thus the return stroke at LEFA 2 is detected approximately 1 ms after the NLDN time, consistent with the 276 km distance between the ground strike point and LEFA 2. The initial sharp-positive step in electric field shown in the figure is to be expected for a +CG return stroke. About 7 ms after the return stroke, the electric field was on average about 0.04 V/m smaller than the electric field before the return stroke (solid horizontal line). For all the sprites, the electric fields before and after the return strokes were very closely matched. This is to be expected because the electrostatic contributions of distant flashes are known to go to zero faster with distance than the field changes caused by current, or current-derivative [*Uman et al.*, 1975].

[25] Note that the electric field oscillates rapidly in the first two milliseconds after the impulse associated with the +CG return stroke. These oscillations are at least partly due to the reflections of the electromagnetic wave generated by the return stroke between the Earth and the ionosphere, the skyhops. The arrival time of a skyhop depends on the location of the ionosphere and on the distance between the strike point and the instrument recording the electromagnetic radiation. The differences in the arrival times of the skyhops are small enough that they are difficult to track with the 50 kHz LEFA instrumentation. The skyhops are clearer in

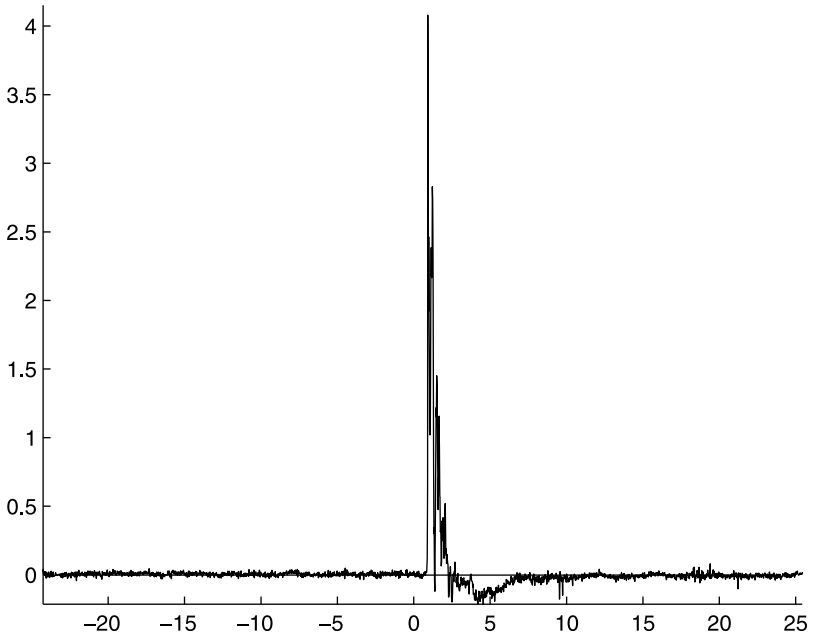

Figure 5. Electric field versus time for sprite 10. Time is measured in milliseconds since the NLDN-reported return stroke at 07:06:09.808870 UT. The solid line shows the average electric field before the return stroke.

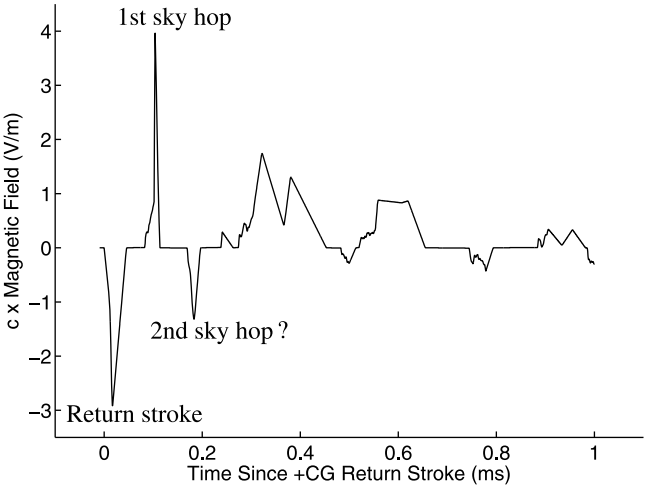

Figure 6. The NLDN waveform recorded near Plano, Texas, for the +CG preceding sprite 10. The time is milliseconds since the arrival of the magnetic field radiation at the instrument.

the magnetic field data from the NLDN, which records the frequency band from 400 Hz to 400,000 Hz.

[26] In Figure 6 we show the magnetic field record associated with sprite 10 recorded by an NLDN instrument located near Plano, Texas, about 670 km southeast of the location of the NLDN reported return stroke for sprite 10. The instrument records north/south and east/west horizontal components of the magnetic field. Figure 6 shows the larger component of the magnetic field. The other component has the same shape, but a smaller amplitude. The instrument only stores waveforms (or "lobes") containing the main features of the wave (onset time, rise-to-peak, significant peaks/valleys) between zero-crossings. This plot was obtained by using linear interpolation between the measured data points. Hence, in the linear segments in the plots, only the end points of the line segment correspond to measured data.

[27] In Figure 6, the first skyhop arrives about 87 μs after the return stroke. Reflection from the ionosphere reverses the sign of the electromagnetic radiation due to the distance between the instrument and the return stroke [*Jacobson et al.*, 2012]. Consequently, the magnetic field associated with the first skyhop is positive. The amplitude of the first skyhop is larger than the amplitude of the original +CG return stroke since the return stroke propagated as a ground wave, which decays with distance more quickly than the sky wave. What appears to be the second skyhop in Figure 6 arrives 166 μs after the return stroke. The second skyhop arrives much sooner than is expected. In particular, the first skyhop's delay corresponds to reflection off a boundary at 87 km altitude. In computing the altitude of the ionosphere associated with the 87 μs delay in the first skyhop, we assumed that the electromagnetic wave traveled at the speed of light c and that the Earth was a sphere with radius r = 6371 km. If the second skyhop also reflected off a boundary at 87 km altitude, then it would be delayed by 291 μs not 166 μs. The apparent early arrival of the second skyhop could be due to its superposition with a ground wave from a different event inside the storm; due to the undersampled data, only this other event is seen, and the second skyhop is missed.

5.2. Return Stroke With Special Sprite Features

5.2.1. Broad Hump Associated With Luminosity

[28] The electric field for sprite 2, shown in Figure 7a, is different from that of the other 9 sprites in the following respect: Between 4 and 8 ms after the +CG return stroke, there is a significant hump in the electric field that closely correlates with a peak in the luminous volume of the sprite recorded by high-speed video (Figure 7b). It also correlates with a hump in the magnetic field shown in Figure 7c.

[29] The Duke VLF magnetic field data for sprite 2 are shown in Figure 7c. The horizontal time axis has been shifted to match the time axis used for the electric field data in Figure 7. We plot the azimuthal magnetic field for a cylindrical coordinate system whose origin is at the location of +CG return stroke preceding the sprite. For far fields, we expect that $B \approx -E/c$. Since the Duke VLF instruments are about 4.75 times as far from the sprite as LEFA 2, the peak in E shown in Figure 7a corresponds to a value of $B \approx \frac{1.45\ \mathrm{V/m}}{4.75\times 3\times 10^8\ \mathrm{m/s}} \approx 1.02$ nT. Referring to the magnetic field plot in Figure 7c, there is reasonable quantitative agreement between the measured magnetic field and the estimated 1.02 nT magnetic field amplitude derived from E.

[30] An electric field hump associated with a sprite was also reported by *Stanley et al.* [2000] where it is referred to as the sprite's signature. In our study, we have excellent agreement between three distinct instruments all applied to the same phenomenon. Note though that only one out of the ten sprites in our study exhibited this hump; the electric field profiles for the other 9 flashes associated with sprites were similar to that shown in Figure 5 for sprite 10. They clearly showed a return stroke waveform, but nothing that could be clearly identified with the sprite.

[31] The hump seen in all panels of Figure 7 will be analyzed in section 9. We will show that modeling a sprite as a downward propagating vertical current pulse reducing the positive charge in the ionosphere can produce just such a hump. Before getting into the mathematical model, we wish to provide a simple, but non-trivial, argument for the sign of the sprite hump.

[32] We assume a sprite is a manifestation of classical breakdown caused by the increased fields above a storm that has just experienced a large positive cloud-to-ground flash. From simple electrostatics, one expects the sprite to bring (effectively) positive charge down from the ionosphere to partly compensate the charge that has just come to ground. A descending positive charge should produce a negative hump in electric field – but we see a positive hump. This is at first a surprise. However, if one treats the ionosphere as a conductor, the descending positive charge is mirrored by an ascending negative charge in the ionosphere. For a distant sprite, the vertical component of the electric field due to the image charge is larger in magnitude than that of the source charge. In more recent work by R. G. Sonnenfeld and W. W. Hager (Electric field reversal in sprite electric field signature, submitted to *Journal of Applied Meteorology*, 2012), it is observed that for sprite 2, the sign of the electric field in the hump should be positive when the distance from the sprite to the instrument is greater than 80 km, while it would be negative when the

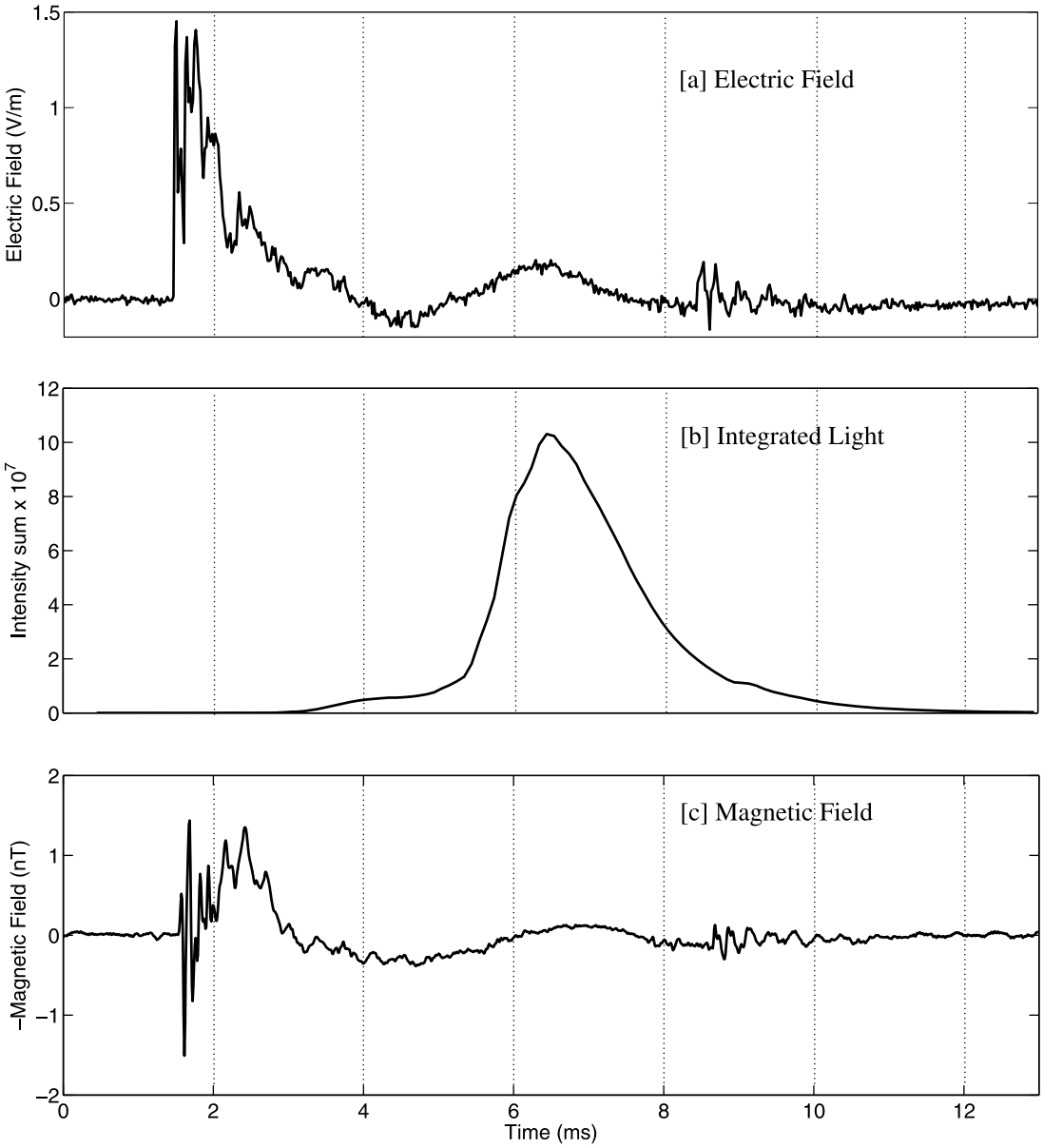

Figure 7. (a) Electric field change, (b) light intensity, and (c) azimuthal magnetic field change versus time for sprite two. Time is measured in milliseconds since the return stroke occurring at 05:27:09.694066 UT. The electric field waveform is delayed by 1.47 ms, the time for the wave to travel 442 km from the NLDN strike point to LEFA 2 at the speed of light. The magnetic field waveform is delayed by more than an additional 6 ms, but this delay has been removed to align E and B. The B-field data is multiplied by −1 to make a peak in E correspond to a peak in B. Since the video camera and E-field sensor are nearly collocated, their relative time references were not adjusted. The light intensity of any frame is obtained by summing the pixel intensities over the entire frame. The units for intensity are arbitrary.

distance is less than 70 km. This electric field reversal connected with the sprite current is related to the well-known [*Rakov and Uman*, 2003, p. 71] electric field reversal associated with dipoles in a cloud. The more rigorous model for the sprite current, which is given in section 9, is based on electrodynamics, not electrostatics.

5.2.2. Oscillations in Electromagnetic Field Toward End of Sprite Luminosity

[33] There is another interesting feature that occurs after the hump in the electric field; the field oscillates for at least a millisecond, beginning around 8.5 ms, when the light from the sprite is still dying out. This oscillation is reminiscent of the oscillations from a lightning return stroke seen at a distance. That is, it looks like a series of impulsive sky waves traveling from a source to the instrument with an increasing number of hops. These oscillations are not local noise, as they are present both in the electric field data Figure 7a and in the magnetic field data in Figure 7c. More convincingly still, the time delays between the return stroke, the hump, and these oscillations are the same in both the electric and

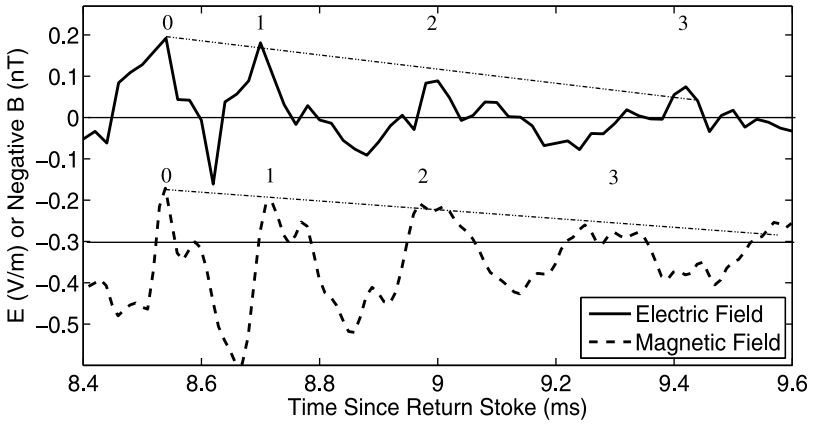

Figure 8. Details of the electric and magnetic field change for the impulsive event that follows the sprite. The first four peaks in the fields are labeled 0, 1, 2, 3. We subtract 0.3 nT from the magnetic field to avoid overlap with the electric field. The dotted line shows that the amplitudes of the peaks decay almost linearly with time as would be expected for waves traveling in free space.

magnetic field measurements. This suggests that the location of the source of these oscillations is at roughly the same location as the return stroke and sprite.

[34] The source of the impulsive event that causes the oscillations following the hump in Figure 7 is somewhat mysterious. We speculate that this event is connected with the reionization of the region in the ionosphere that was receiving the sprite current. It is known that lightning channels re-ionize (K-changes, M-components, etc.), and there is no reason to suppose that an ionization wave from a sprite might not also have impulsive components.

5.2.3. Electromagnetic Evidence of Reduced Height of Ionosphere Over MCS

[35] Figure 8 shows the electric and magnetic fields during the impulsive event that follows the sprite. The arrival times of the peaks (1, 2, and 3) in the oscillations, relative to the first peak (0), are 160 μs, 460 μs, and 880 μs. Using a purely geometric model in which impulses bounce off of reflecting ground and ionosphere, we can calculate that this peak spacing is consistent with reflections off a shell at 44 km altitude as the electric field travels west from the storm to LEFA 2. A 44 km shell yields modeled time differences of 165 μs, 497 μs, and 927 μs, respectively. In contrast, a more typical ionosphere at 85 km altitude yields modeled time differences of 542 μs, 1441 μs, and 2463 μs.

[36] Figure 8 includes a dotted line which shows that the decay of the peak amplitudes are nearly linear in time. For a series of sky waves traveling to the instrument with different numbers of hops, the arrival times also provide a measure of the distance traveled by the sky wave. In free space, the amplitude of an electromagnetic radiation wave is expected to decay linearly with distance. As we saw in Figure 6, the ground wave associated with the return stroke attenuated much more quickly than the first sky hop. For an impulsive event that occurs near ground, the first peak in the transmitted wave, associated with the ground wave, should have an exceptional amplitude unlike that of the sky hops which are traveling through free space. In Figure 8, the amplitude of the first peaks fits nicely with the linear tread which is evidence that the impulsive event did not occur near ground.

[37] For the magnetic field in Figure 8, the arrival times of the peaks 1, 2, and 3 relative to the first peak 0 are 180 μs, 430 μs, and 710–800 μs relative to the first peak of oscillation. For a wave propagating east from the strike point of the parent stroke for sprite 2 to the B-field instruments at Duke 2098 km away, we obtain an ionosphere between 79 and 84 km: the modeled delays are 147 μs, 415 μs, and 815 μs for a 79 km ionosphere and 162 μs, 463 μs, and 912 μs for an 84 km ionosphere.

[38] One wonders why the electric field data is roughly fit by a very low (around 45 km) ionosphere while the magnetic data is fit by a more typical 80–85 km ionosphere. Figure 1 reminds us that a wave propagating from sprite 2 to LEFA 2 travels mostly over the MCS, whereas the path of the B-field signal is over mostly clear skies. A possible explanation for the apparent lowering of the ionosphere above the MCS is given by *Lehtinen and Inan* [2007]. They present a five constituent model of stratospheric/lower-ionosphere chemistry and observe that giant blue jets can cause substantial ionization which exhibits a long recovery period of more than 10 minutes. It is pointed out that a similar ionization could be caused by large sprites. Note that *Haddad et al.* [2012] reports a lowering of the ionosphere following the first stroke in a multistroke flash, from about 81 km down to 76 km for 103 out of 124 flashes [see *Haddad et al.,* 2012, Figure 8], and from about 81 km down to 70 km for all flashes.

6. Electromagnetic Radiation From a Finite Antenna

[39] The analysis of the sprite electric field hump seen in Figure 7 is based on the exact solution to Maxwell's equation given by *Uman et al.* [1975] for a vertical antenna on a perfectly conducting ground plane. Generalizations of this formula can be found in *Master et al.* [1981], *Master and Uman* [1983], and *Uman* [1987]. *Lu* [2006] gives an application to the study of the fields near elves from a lightning

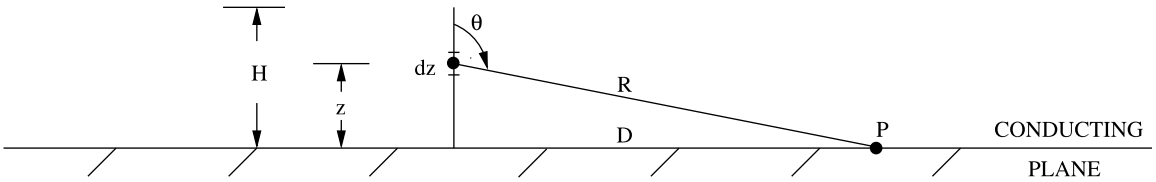

Figure 9. A vertical antenna of height H above a perfectly conducting ground plane.

return stroke. The geometry considered in *Uman et al.* [1975] is shown in Figure 9, where the z-axis is perpendicular to the conducting ground plane, the current is $i(z,t) = 0$ for $t \le 0$, and H is the height of the antenna. It was shown that the vertical electric field $E(t)$ at time t and observation point P on the conducting ground plane can be expressed

$$E(t) = \frac{1}{2\pi\varepsilon_0}\left[\int_0^H \int_0^t \left(\frac{2-3\sin^2\theta(z)}{R(z)^3}\right) i\left(z, \tau - \frac{R(z)}{c}\right) d\tau dz + \int_0^H \left(\frac{2-3\sin^2\theta(z)}{cR(z)^2}\right) i\left(z, t - \frac{R(z)}{c}\right) dz - \int_0^H \frac{\sin^2\theta(z)}{c^2 R(z)} \frac{\partial i(z, t - R(z)/c)}{\partial t} dz\right]. \quad (1)$$

The three terms on the right side of the equation are often called the electrostatic term, the induction term, and the radiation term. If D denotes the distance from the observation point P to the base of the antenna, then $R(z) = \sqrt{D^2 + z^2}$ and $\sin\theta(z) = D/R(z)$. The formula (1) was derived by combining the fields associated with a dipole current source with the fields associated with an opposite charged (image) dipole current beneath the surface of the Earth. We note that image charge techniques developed for the electrostatic field associated with a conducting sphere do not extend to time varying electromagnetic fields so the planar geometry associated with (1) is an important requirement.

7. Treatment of a Second Parallel Conducting Plane

[40] The formula (1) takes into account the boundary condition associated with a perfectly conducting ground plane, however, it does not account for the boundary condition at the ionosphere, which is relatively highly conductive. We approximate the ionosphere as a perfectly conducting plane, and we consider a vertical antenna with a current traveling from height $z = z_0$ up to the ionosphere $z = H$ (see Figure 10). We derive the analogue of (1) that takes into account two perfectly conducting boundary conditions, a conducting ground plane $z = 0$ and a conducting plane at $z = H$ corresponding to the ionosphere. We associate with a small current dipole of length dz at altitude z, a series of image dipoles (see Figure 11). There are subterranean images S_k (below the ground), and ionospheric images I_k (altitude larger than H), where $k \ge 1$ is an integer. The subterranean image S_1 at altitude $-z$ is the reflection of the source S at altitude z across the ground plane. The image I_1 at altitude $2H - z$ is the reflection of the source S across the ionosphere plane. The subterranean image S_1 generates an ionospheric image I_2 at $2H + z$, the reflection of S_1 across the ionosphere plane. The ionospheric image I_1 generates a subterranean image S_2 at altitude $-(2H - z)$, the reflection of I_1 across the ground plane.

[41] The process depicted in Figure 11 is summarized in the flowchart of Figure 12. The original source S generates two images, S_1 and I_1 gotten by reflection across the ground plane and the ionosphere plane. S_1 generates I_2 by reflection across the ionosphere plane, and I_1 generates S_2 by reflection across the ground plane. The process of generating images continues as depicted in Figure 12. If the original source S is a positive dipole generator, then S_1 and I_1 are negative and S_2 and I_2 are positive, each reflection flips the sign.

[42] As indicated in Figure 11, we let $R_k(z)$ denote the distance from P to the subterranean image S_k. Referring to Figure 11, we have $R_k(z) = \sqrt{D^2 + z_k^2}$ where

$$z_k = \begin{cases} kH - z & \text{if } k \text{ is even,} \\ kH + z - H & \text{if } k \text{ is odd.} \end{cases}$$

Moreover, $\sin\theta_k(z) = D/R_k(z)$. We now combine the images in special way in order to exploit the formula (1) for the electric field of a vertical antenna on a conducting ground plane. We first consider the pair of images on either end of the G arrows in Figure 12, namely $(+S,-S_1)$, $(-I_1,+S_2)$, $(+I_2,-S_3)$, $(-I_3,+S_4)$, and so on. When k is even, I_k is flagged with + and when k is odd, I_k is flagged with −. The image S_{k+1} is obtained from the image I_k by reflection across the ground

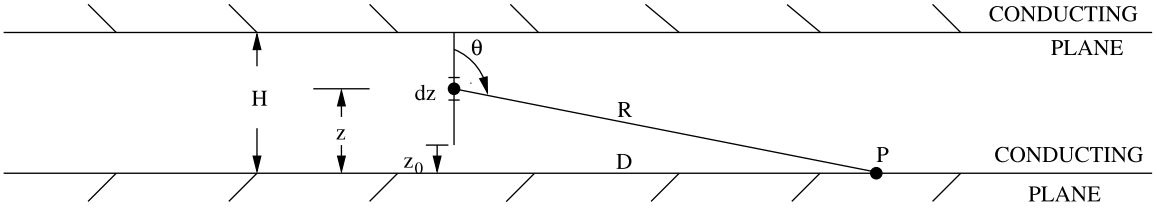

Figure 10. A vertical antenna situated between perfectly conducting planes at the ionosphere $z = H$ and at the ground $z = 0$.

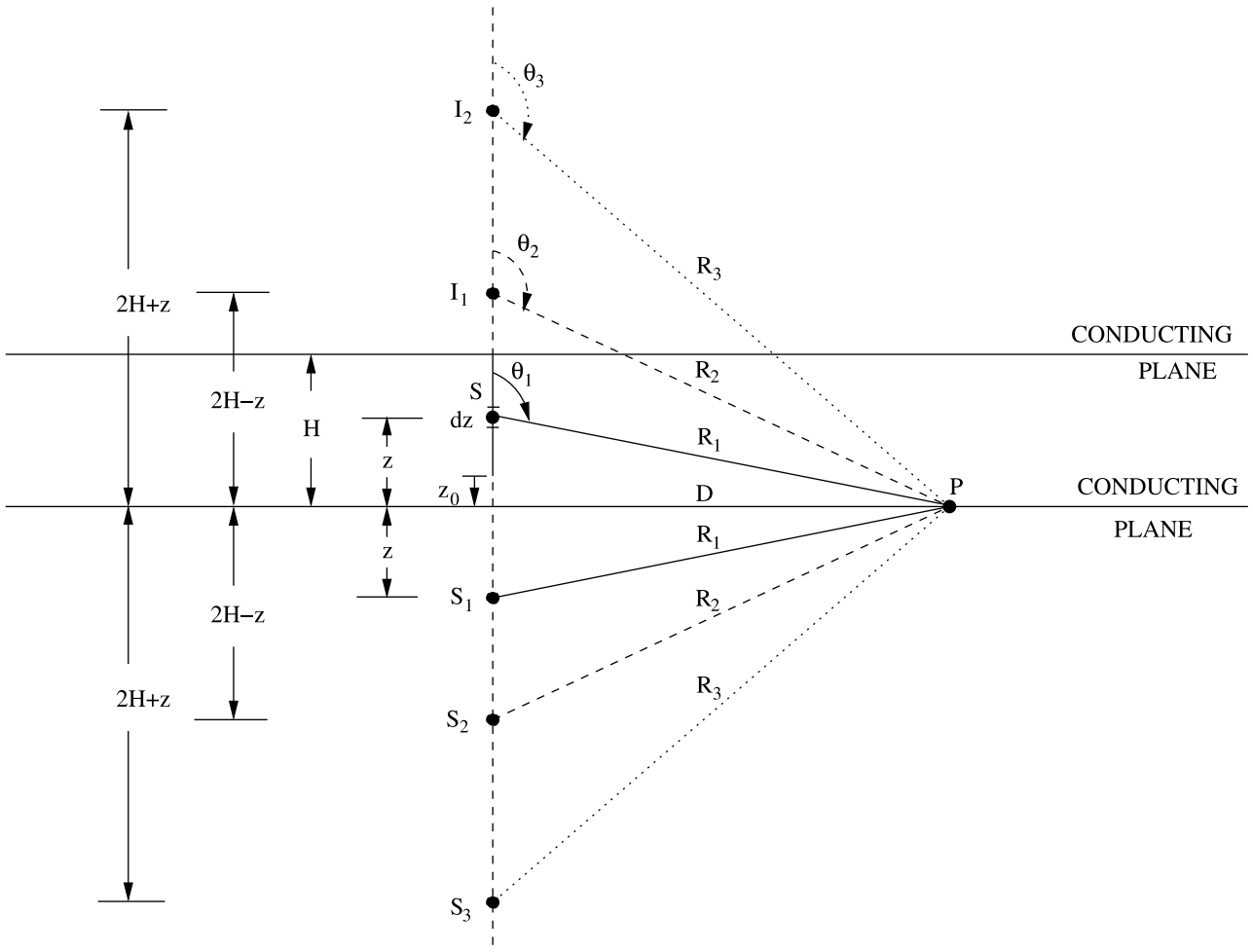

Figure 11. The image dipoles generated by the source dipole current at altitude z. S_1 is the image of S relative to the ground plane and I_1 is the image of S relative to the ionospheric plane. For $k > 1$, S_k is the subterranean image associated with I_{k-1} above the ionosphere.

plane. Since each of these image pairs (I_k,S_{k+1}) is associated with a ground reflection, we can apply the formula (1) to obtain the associated electric field:

$$E_k(t) = \frac{(-1)^{k+1}}{2\pi\varepsilon_0}\left[\int_{z_0}^{H}\int_0^t \left(\frac{2-3\sin^2\theta_k(z)}{R_k(z)^3}\right) i\left(z, \tau - \frac{R(z)}{c}\right) d\tau dz + \int_{z_0}^{H}\left(\frac{2-3\sin^2\theta_k(z)}{cR_k(z)^2}\right) i\left(z, t-\frac{R(z)}{c}\right) dz - \int_{z_0}^{H}\frac{\sin^2\theta_k(z)}{c^2R_k(z)}\frac{\partial i(z, t-R(z)/c)}{\partial t} dz\right] \quad (2)$$

The total electric field E at the observation point P is simply the sum of the E_k:

$$E(t) = \sum_{k=1}^{\infty} E_k(t). \quad (3)$$

The series for E is convergent since the terms are bounded by C/k^2 for some constant C. The boundary conditions for a perfect conductor on the ground plane $z = 0$ are satisfied since each term in the sum satisfies the boundary conditions for a perfect conductor on the ground plane.

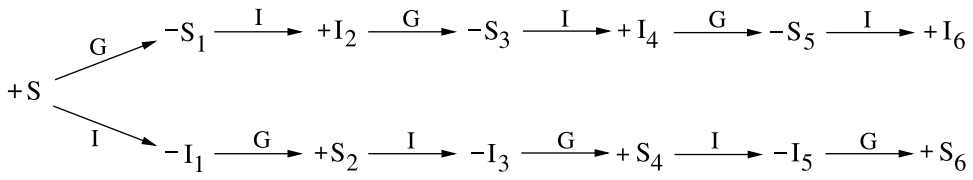

Figure 12. A flowchart showing how the subterranean and ionospheric images of Figure 11 propagate. The sign of the dipoles flip with each reflection. We place a *G* or an *I* above an arrow to denote a ground or an ionospheric reflection respectively.

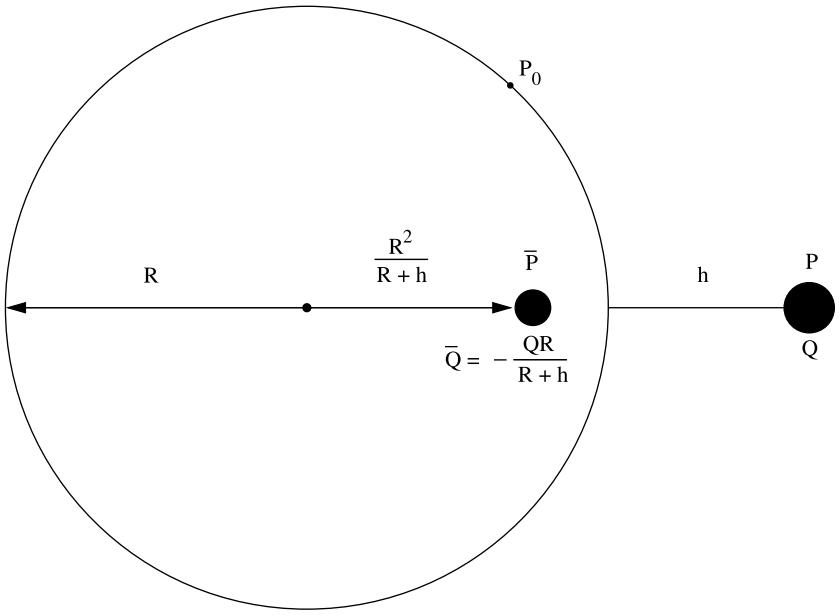

Figure 13. The method of images for determining the electric field at a point P_0 on the surface of a perfectly conducting sphere due to a charge Q at a distance h outside the sphere. $\overline{P}$ is the image of P.

[43] We now show that the expression (3) also satisfies the boundary conditions for a perfect conductor at $z = H$, the ionosphere. The formula (1) was derived by combining a dipole current generator above the ground plane $z = 0$ with an opposite charged dipole current generator below the ground plane. Hence, two terms were used to form the expression (1). We can think of (3) as representing the following symbolic sum:

$$E(t) = (S - S_1) + (S_2 - I_1) + (I_2 - S_3) + (S_4 - I_3) + (I_4 - S_5) + \cdots.$$

corresponding to the ground pairs in Figure 12:

$$(+S, -S_1), \quad (-I_1, +S_2), \quad (+I_2, -S_3), \quad (-I_3, +S_4), \quad \cdots.$$

In other words, the expression (1) is the difference of two terms, a source term above the ground plane and a mirror image below the ground plane, and each of the terms (2) in (3) has this same form.

[44] Now, let us regroup the terms forming $E(t)$ using the ionospheric pairs in Figure 12:

$$(+S, -I_1), \quad (-S_1, I_2), \quad (+S_2, -I_3), \quad (-S_3, +I_4), \quad (+S_4, -I_5), \cdots.$$

This rearrangement of the images leads to a small rearrangement of the terms forming $E(t)$:

$$E(t) = (S - I_1) + (I_2 - S_1) + (S_2 - I_3) + (I_4 - S_3) + (S_4 - I_5) + \cdots.$$

This rearrangement does not change the sum; moreover, each term in the sum satisfies the boundary conditions for a perfect conductor at the ionosphere. That is, as can be seen in Figure 11, I_1 is the image of S relative to the ionosphere, S_1 is the image of I_2 relative to the ionosphere, and so on. Each term in the sum consists of a subterranean image S_k and its reflection I_{k+1} in the ionosphere. Since each term satisfies the boundary conditions for a perfect conductor at the ionosphere, so does the entire sum.

8. Analysis of the Image Charge

[45] In practice, the infinite series in (3) must be terminated when k is sufficiently large. In this section we analyze both the flat Earth approximation used in the previous section and the effect of truncating the sum in (3). To help understand these two approximations, we focus on a well understood problem: Compute the electric field above the surface of a conducting sphere. Referring to Figure 13, we would like to determine the electric field at a point P_0 on the surface of a perfectly conducting sphere due to a point charge Q at location P, a distance h outside the sphere. The solution is obtained by the method of images: We introduce an additional charge $\overline{Q} = -QR/(R + h)$ at location $\overline{P}$, a distance $R^2/(R + h)$ from the center of the sphere. The electric field E_0 at P_0 is the sum of the electric field due to the original charge Q at location P, and the electric field due to the image charge $\overline{Q}$ at location $\overline{P}$:

$$E_0 = \frac{1}{4\pi\epsilon_0}\left[\frac{Q(P_0 - P)}{\|P_0 - P\|^3} + \frac{\overline{Q}(P_0 - \overline{P})}{\|P_0 - \overline{P}\|^3}\right]. \tag{4}$$

Here $\|\cdot\|$ denotes the Euclidean norm. Since the electric field on the surface of a perfectly conducting sphere is perpendicular to the surface of the sphere, an electric field meter placed at P_0 on the surface of the sphere would experience a vertical electric field (perpendicular to the surface of the sphere) of magnitude $\|E_0\|$.

[46] If there is a second conducting sphere surrounding the sphere of Figure 13, then there is not only the image $\overline{P}$ of P

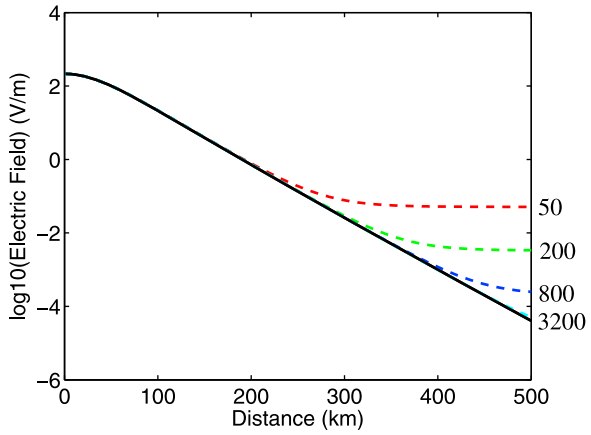

Figure 14. The base 10 log of the electric field as a function of distance from an electric field meter for a −100 C point charge 75 km above the surface of the Earth. The Earth and the ionosphere are treated as perfectly conducting spheres of radii 6,371 km and 6,471 km respectively. The solid curve corresponds to a spherical Earth and ionosphere. The dashed curves correspond to a flat Earth, an ionosphere 100 km above the surface of the Earth, and to either 50, 200, 800, or 3200 image pairs in the approximation to the electric field.

inside the inner sphere, but also an image $\overline{\overline{P}}$ of P outside the surrounding sphere. And each of these images generates images as in section 7, leading to an infinite sequence of images. For each pair of images, the electric field is given by an expression of the form (4). The total electric field is given by this infinite series consisting of terms of the form (4).

[47] Figure 14 plots the electric field due to a −100 C point charge at an altitude of 75 km as a function of the great circle distance on the surface of the Earth to the point where we measure the electric field. We treat the Earth as a perfectly conducting sphere of radius 6,371 km, and we treat the ionosphere as a perfectly conducting spherical shell of radius 6,471 km (100 km above the surface of the Earth). The horizontal axis in Figure 14 gives the great circle distance from the electric field sensor to the charge location on the Earth, the vertical axis is the base 10 log of the electric field (V/m), and the solid black curve shows the electric field as a function of distance. Observe that the base 10 log of the electric field in Figure 14 is nearly a linearly function of distance. This implies that $E \approx c10^{-\alpha D}$ where $-\alpha$ is the slope of the line in Figure 14.

[48] This exponential decay of the electric field with distance is nonintuitive. For a single image charge, as in (4), the decay of the electric field is proportional to $1/D^3$ for P_0 near P. The $1/D^3$ corresponds to the small bend at the top of the curve in Figure 14. When D is greater than 50 km, the curve is essentially linear. This transition from $1/D^3$ to $10^{-\alpha D}$ is due to the infinite sequence of image charges produced by the ionosphere. There is cancelation in the series causing the electric field to decay exponentially fast instead of like $1/D^3$.

[49] Next, we repeat this computation of the electric field, but with the spherical Earth and ionosphere replaced by a flat Earth and ionosphere. The formula for the electric field is again given by (4), but with $\overline{Q} = -Q$ and with $\overline{P}$ the mirror image of P in the ground plane. Again, there is an infinite sequence of image charges. The dashed curves in Figure 14 were obtained by terminating the electric field computation after a different number of image charge pairs. We consider 50, 200, 800, and 3200 image charge pairs. The solid curve in Figure 14 for a spherical Earth, obtained using 80 image pairs, is correct to 16 digits. It is clear from Figure 14 that the series for the electric field on a flat Earth converges much more slowly than the series for the electric field on a spherical Earth. Nonetheless, the field gotten from the flat Earth model is very close to field gotten with the spherical Earth model if we include enough terms in the sum. Based on Figure 14, the flat Earth approximation to the electric field on the surface of a sphere is correct to 1 digit accuracy at 500 km if we use 3200 image pairs.

[50] In Figure 14 we focus on a point charge at an altitude of 75 km. When we vary the altitude of the charge, we obtain similar plots. Figure 15 plots the base 10 log of the electric field for the same −100 C charge at 3, 10, and 50 km altitude. Observe that in each case, the plot approaches a line of the same slope. By fitting the plots with straight lines, we deduce that the vertical electric field (V/m) on the surface of the Earth is given by

$$E = -Qc(h)10^{-\alpha D}, \quad \alpha = (.014093 \pm 0.000002)/\text{km},$$
$$c(h) = \sum_{i=0}^{4} a_i h^i, \tag{5}$$

where D is the great circle distance from the sensor to the charge in kilometers, h is the height of the charge in kilometers, and the coefficients a_i have the following values:

$$a_0 = \quad 4.84546\text{e}{-3} \quad a_1 = 2.00712\text{e}{-1} \quad a_2 = 2.32032\text{e}{-4}$$
$$a_3 = -4.53918\text{e}{-5} \quad a_4 = 2.30095\text{e}{-7}$$

9. Current Model for Sprite Charge Transport

[51] We now apply the model developed in section 7 to the interval of electric field that correlates with the light

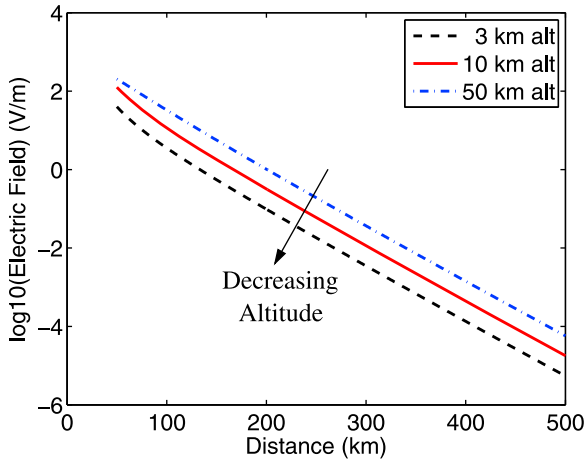

Figure 15. The base 10 log of the electric field as a function of distance from the electric field meter for a −100 C charge placed at different altitudes above the surface of the Earth. The Earth and the ionosphere are treated as perfectly conducting spheres of radii 6,371 km and 6,471 km respectively.

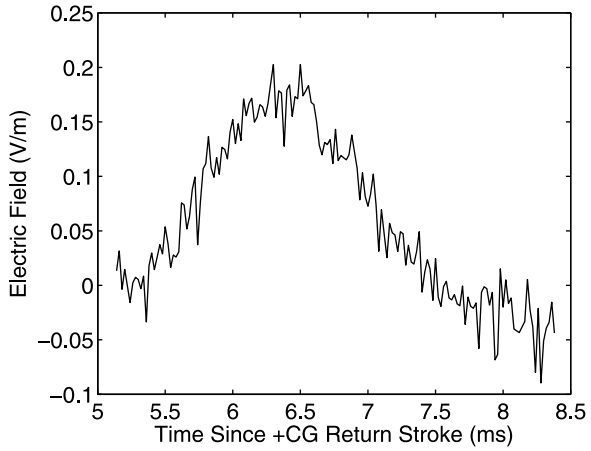

Figure 16. The electric field at LEFA 2 which correlates with the light from sprite 2.

emitted by sprite 2. According to the conventional breakdown theory for sprites [*Pasko et al.*, 1997], the light emitted by the sprite corresponds to regions of the atmosphere that were ionized by the electric field. To the extent that the ionized channel is an equipotential, it will have a polarization charge on either end, and as the ionization spreads to lower altitudes, it looks like a descending positive current. We believe that the electric field hump corresponds to this ionization current since the amplitude of the hump almost exactly matches the light intensity of the sprite.

[52] Our application of the model developed in section 7 entails several approximations:

[53] 1. *We approximate the ionosphere as a perfect conductor.* The conductivity of the ionosphere ranges from 10^{-7} to 10^{-4} siemens/m which is orders of magnitude greater than the conductivity of air (3.0×10^{-15} up to 10^{-13} siemens/m) near the surface of the Earth [*Pawar et al.*, 2009; *U.S. Air Force*, 1960].

[54] 2. *The surface of the Earth is approximated by a flat plane.* The distance between LEFA 2 and the sprite in this storm is about 442 km. Since an object 442 km away drops about 15 km beneath the horizon due to the curvature of the Earth, LEFA 2 should have a line-of-sight view of the sprite. Moreover, the analysis of section 8 indicates that by including enough image charges, the flat Earth approximation is still relatively accurate.

[55] 3. *The current transport in the sprite is approximated by that of an infinitely small wire.* The diameter of the sprite is small relative to the distance between LEFA 2 and the sprite.

[56] 4. *The current can be approximated by a current pulse that maintains the same shape as it propagates at constant speed on the wire.* This *transmission line model* has been applied to lightning return strokes for years, but not to sprites. It is not claimed that sprite streamers are transmission lines, only that the current pulse propagates at constant speed without changing shape. The current pulse is the propagation of classical breakdown. This is clearly an approximation whose main virtue is that it allows us to calculate a speed and a current waveform. The conductivity of a sprite streamer is many orders of magnitude lower than a return stroke, but the channel area is also many orders of magnitude larger, so the peak currents are still kiloamps, as will be seen.

[57] 5. *Conduction current in the air above the cloud is neglected.* Since the electric field hump in Figure 7 associated with the light from the sprite only lasts for a few milliseconds, the negative charge transport that can be accomplished by conduction is a fraction of the negative charge transport possible on a highly conductive lightning channel.

[58] A plot of the electric field used in the analysis is shown in Figure 16. The length of the electric field interval is about 3 ms. It begins when the electric field reaches 0 in Figure 7, and it continues until the end of the hump, just before the large oscillations that occur at the end of the sprite current pulse.

[59] The video of sprite 2 shows an initial broad glow extending from 70 to 85 km. Based on measurements in the video records, the first three carrots initiate roughly between 68 and 71 km altitude, 67 and 74 km altitude, and 70 and 74 km altitude. These altitudes are in good agreement with the location for the head of a carrot sprite given as 66 to 74 km (±4 km) altitude by *Sentman et al.* [1995]. The luminosity wave proceeds downward to about 60 km, then suddenly blooms in both directions, proceeding back up to the ionosphere and down to about 50 km altitude. Sprite researchers have long assumed that the extent of the luminosity wave indicates the extent of the ionized region [*Pasko et al.*, 1997]. In our analysis, we also assume that the region illuminated by the sprite corresponds to the region where the atmosphere is ionized.

[60] In approximating the electric field using the model developed in section 7, we truncate the sum (3) after 3200 terms. We place the ionosphere at an altitude 100 km above that of LEFA 2. The sprite current is assumed to transport charge along a channel that extend from $z_0 = 50$ km (the bottom of the sprite) up to the ionosphere (the top of the sprite). The current i is modeled as in a transmission line [see *Uman and McLain*, 1969]:

$$i(z,t) = i(t + z/v),$$

where z is altitude and v is the velocity of the downward descending current pulse.

[61] Since we do not know the propagation velocity, we tried different velocities to see how well we could fit the measured electric field. For velocities below 0.1 c, the agreement with measurements was relatively poor. Possibly, the reason for the poor agreement when the velocity is below 0.1 c is that the current wave needs at least this much speed to traverse the distance from the ionosphere to the bottom of the sprite during the time interval of the electric field hump. Hence, we focused on velocities of at least 0.1 c. We give results for the three velocities 0.25 c, 0.40 c, and 0.55 c. *Rakov and Uman* [2003] in Chapter 1 of their book suggest velocities for return strokes of CGs on the order of 1 to 2×10^8 m/s. *Idone and Orville* [1982] report a mean velocity for the return stroke of 1.1×10^8 m/s (about 0.37 c) The current pulse velocities that yield reasonable fits to the data appear to be consistent with the measured velocity of a return stroke for cloud-to-ground lightning.

[62] The width of the current pulse is chosen so that the corresponding electric field pulse detected by LEFA 2 has the width seen in Figure 16. The current pulse is approximated by a piecewise linear spline with 20 equally spaced knots. For each current pulse velocity, we compute the

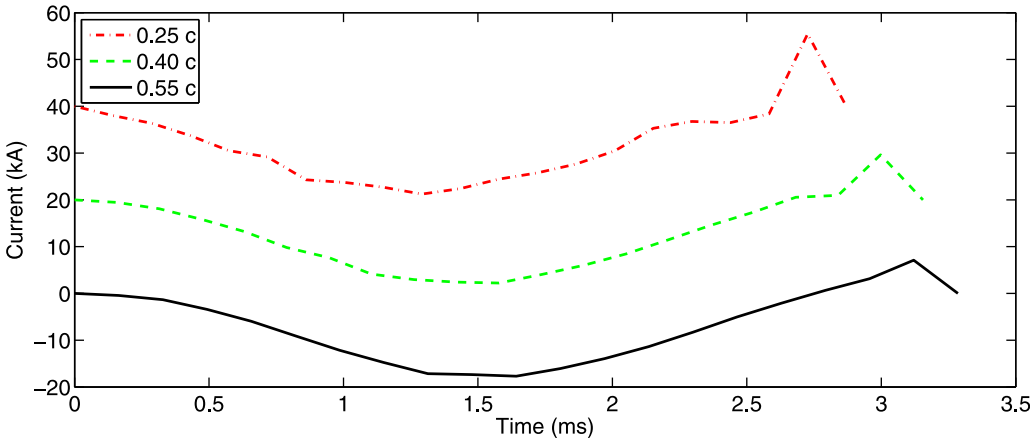

Figure 17. The sprite current at the top of the sprite channel (the ionosphere) as a function of time; the three plots correspond to three different velocities for the current wave traveling along the sprite channel. The plot for velocity 0.40 c is shifted up by 20 kA, while the plot for velocity 0.25 c is shifted up by 40 kA.

current *i* that results in the best least squares fit to the measured electric field data at LEFA 2.

[63] In Figure 17 we show the best fitting current pulse for the three velocities. The plots give the current at the ionosphere as a function of time. The slower pulses were shifted up by 20 kA and 40 kA to avoid overlap of the plots. For the transmission line model, the current at any altitude between the bottom of the sprite and the ionosphere would be the same as the current at the top of the channel (the ionosphere), but delayed by the time it takes the pulse to travel to that altitude. The peak current for the current pulse traveling at 0.55 c is −17.7 kA, which is larger in magnitude than the 3.3 kA, 3.3 kA, and 1.6 kA currents obtained by *Cummer et al.* [1998] for 3 different sprites, but less than the 25 kA current obtained for a sprite in *Cummer* [2003]. Note that the techniques used to recover the sprite current here are quite different from earlier techniques to recover a sprite current, as described in *Li et al.* [2008] and *Hu and Cummer* [2006]. Here we use an exact solution to Maxwell's equation that approximates a sprite as a thin, perfectly conducting wire. The techniques in *Li et al.* [2008] and *Hu and Cummer* [2006] are based on finite difference approximations to Maxwell's equation and a deconvolution method described in *Cummer and Inan* [2000]. In our approach, we need to provide the start and end of the channel along which the current propagates. In the techniques developed in *Li et al.* [2008], *Hu and Cummer* [2006], and *Cummer and Inan* [2000], a current moment is computed, and then from the length of the channel, a current is obtained.

[64] In Figure 18, we compare the modeled electric field to the measured electric field at LEFA 2 for the current pulse traveling at 0.40 c. Each of the current pulses shown in Figure 17 fit the measured electric field with comparable accuracy. In Figure 19, we decompose the modeled electric field for the current pulse traveling at 0.4 c into its three components, the electrostatic field, the induction field, and the radiation field. The radiation component of the electric field accounts for the fastest changes in the field; initially the electric field is essentially the radiation component. As time progresses, the induction term becomes more significant. The electrostatic component grows slowest; it is the smoothest component of the electric field.

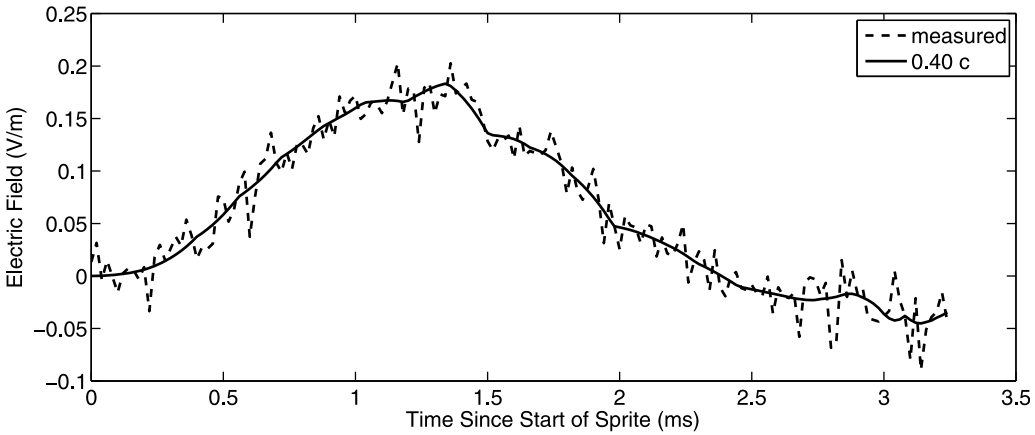

Figure 18. Comparison between the measured electric field at LEFA 2 and the modeled electric field for the current pulse traveling at 0.40 c.

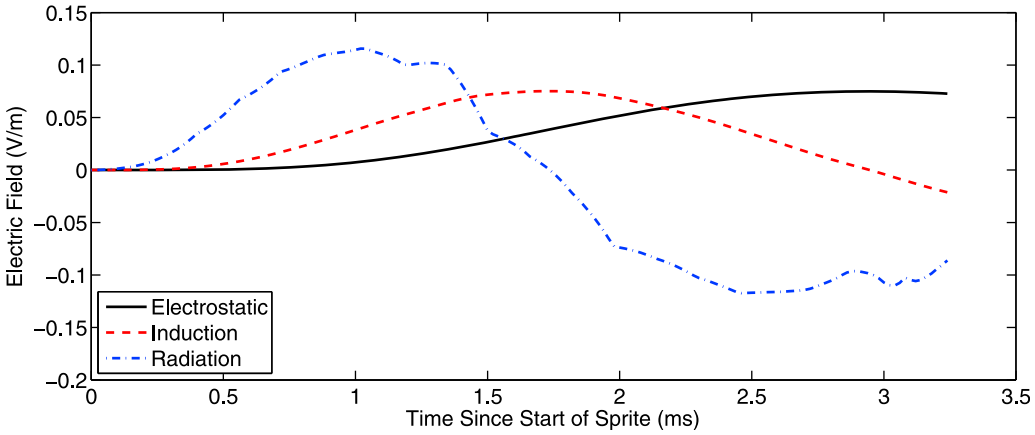

Figure 19. The electric field associated with the current pulse of Figure 17 traveling 0.40 c is decomposed into its three components, the electrostatic field, the induction field, and the radiation field. These three components correspond to the three terms in equation (1).

[65] Table 3 gives the charge transported by the three current pulses shown in Figure 17. It is obtained by integrating the current. For comparison *Cummer et al.* [1998] estimate the charge transport to the ionosphere for 3 sprites in their study as 5 C, 6 C, and 42 C assuming 50% of the total charge transport went to the ground and 50% went to the ionosphere. Our analysis is different in that we are just estimating the charge transported from the ionosphere.

10. Conclusions

[66] In summary, we provided very clear evidence of an electromagnetic signature associated with a sprite, with excellent correlation between E-field, B-field and high-speed video measurements. Further, we showed that the hump in the electric field that followed the return stroke of a sprite producing +CG, sprite 2, could be modeled by a current pulse that traveled vertically through the volume illuminated by the sprite. We adapted a transmission line model which has been routinely applied to lightning return strokes and changed the boundary conditions to apply it to sprites by including two conducting boundaries (ionosphere and ground). Using the transmission line model and a pulse velocity between 0.25 c and 0.55 c, the charge transport to the ionosphere was about 23.9 C. For 9 out of the 10 sprites in our study, any current pulse associated with the sprite was so small that it could not be measured. *Cummer* [2003] also remarked that approximately 10% of all sprites contain a clear sprite current ELF signature, so our results are consistent with those.

[67] Finally, we noticed a tantalizing impulsive electromagnetic disturbance that followed the sprite current and was visible in the final stages of sprite luminosity. While a lightning channel regularly shows such current pulses late in a flash (K-changes), we believe this to be the first observation of such a signature in a sprite. The oscillations associated with the impulsive event corresponded to reflections between the Earth and a shell at altitude 45 km above the MCS and at an altitude of 80 to 85 km outside the MCS.

Table 3. Charge Transport for the Current Pulses Plotted in Figure 17

Velocity	Charge (C)
0.25 c	−24.0
0.40 c	−23.9
0.55 c	−23.9

[68] **Acknowledgments.** This work was funded by grants 0619080, 0724750, 0724771, 0737294, 0737605, 1042198, and 1047588 from the National Science Foundation. Additional funding was provided by the DARPA NIMBUS program and by the Irving and Marion Langmuir bequest to Langmuir Laboratory. We thank Tsutomu Takahashi for asking a basic question about what sign is to be expected for the sprite hump, and we thank Vladimir Rakov for pointing out the sign dependence of a sky wave with respect to distance between instrument and return stroke. The authors thank Vaisala Inc for providing high accuracy strike data from the National Lightning Detection Network (NLDN) as well as data for Figure 6. Kenneth L. Cummins is especially acknowledged for his help in interpreting NLDN data and in accessing the NLDN waveforms. Comments from the reviewers, which improved the manuscript, are gratefully appreciated.

References

Bell, T. F., V. P. Pasko, and U. S. Inan (1995), Runaway electrons as a source of red sprites in the mesosphere, *Geophys. Res. Lett.*, *22*, 2127–2130.

Boccippio, D. J., E. R. Williams, S. J. Heckman, W. A. Lyons, I. T. Baker, and R. Boldi (1995), Sprites, ELF transients, and positive ground strokes, *Science*, *269*, 1088–1091.

Crum, T. D., and R. L. Alberty (1993), The WSR-88D and the WSR-88D operational support facility, *Bull. Am. Meteorol. Soc.*, *74*, 1669–1687.

Crum, T. D., R. L. Alberty, and D. W. Burgess (1993), Recording, archiving, and using WSR-88D data, *Bull. Am. Meteorol. Soc.*, *74*, 645–653.

Crum, T. D., R. E. Saffle, and J. W. Wilson (1998), An update on the NEXRAD program and future WSR-88D support to operations, *Weather Forecasting*, *13*, 253–262.

Cummer, S. A. (2003), Current moment in sprite-producing lightning, *J. Atmos. Solar Terr. Phys.*, *65*, 499–508.

Cummer, S. A., and U. S. Inan (1997), Measurement of charge transfer in sprite-producing lightning using ELF radio atmospherics, *Geophys. Res. Lett.*, *24*, 1731–1734.

Cummer, S. A., and U. S. Inan (2000), Modeling ELF radio atmospheric propagation and extracting lightning currents from ELF observations, *Radio Sci.*, *35*, 385–394.

Cummer, S. A., and W. A. Lyons (2005), Implications of lightning charge moment changes for sprite initiation, *J. Geophys. Res.*, *110*, A04304, doi:10.1029/2004JA010812.

Cummer, S. A., and M. Stanley (1999), Submillisecond resolution lightning currents and sprite development: Observations and implications, *Geophys. Res. Lett.*, *26*, 3205–3208.

Cummer, S. A., U. S. Inan, T. F. Bell, and C. P. Barrington-Leigh (1998), ELF radiation produced by electrical currents in sprites, *Geophys. Res. Lett.*, *25*, 1281–1284.

Cummins, K. L., and M. J. Murphy (2009), An overview of lightning locating systems: History, techniques, and data uses, with an in-depth look at the U.S. NLDN, *IEEE Trans. Electromagn. Compat.*, *51*, 499–518.

Franz, R. C., R. J. Nemzek, and J. R. Winckler (1990), Television of a large upward electrical discharge above a thunderstorm system, *Science*, *249*, 48–51.

Haddad, M. A., V. A. Rakov, and S. A. Cummer (2012), New measurements of lightning electric fields in Florida: Waveform characteristics, interaction with the ionosphere, and peak current estimates, *J. Geophys. Res.*, *117*, D10101, doi:10.1029/2011JD017196.

Hu, W., and S. A. Cummer (2006), An FDTD model for low and high altitude lightning-generated EM fields, *IEEE Trans. Antennas Propag.*, *54*(5), 1513–1522.

Idone, V. P., and R. E. Orville (1982), Lightning return stroke velocities in the Thunderstorm Research International Program (TRIP), *J. Geophys. Res.*, *87*, 4903–4915.

Jacobson, A. R., X.-M. Shao, and E. Lay (2012), Time domain waveform and azimuth variation of ionospherically reflected VLF/LF radio emissions from lightning, *Radio Sci.*, *47*, RS4001, doi:10.1029/2012RS004980.

Klazura, G. E., and D. A. Imy (1993), A description of the initial set of analysis products available form the NEXRAD WSR-88D system, *Bull. Am. Meteorol. Soc.*, *74*, 645–653.

Lehtinen, N. G., and U. S. Inan (2007), Possible persistent ionization caused by giant blue jets, *Geophys. Res. Lett.*, *34*, L08804, doi:10.1029/2006GL029051.

Li, J., S. A. Cummer, W. A. Lyons, and T. E. Nelson (2008), Coordinated analysis of delayed sprites with high-speed images and remote electromagnetic fields, *J. Geophys. Res.*, *113*, D20206, doi:10.1029/2008JD010008.

Lu, G. (2006), Transient electric field at high altitudes due to lightning: Possible role of induction field in the formation of elves, *J. Geophys. Res.*, *111*, D02103, doi:10.1029/2005JD005781.

MacGorman, D. R., and W. D. Rust (1998), *The Electrical Nature of Thunderstorms*, 422 pp., Oxford Univ. Press, New York.

Master, M. J., and M. A. Uman (1983), Electric and magnetic fields associated with establishing a finite electrostatic dipole: An exercise in the solution of Maxwell's equation, *Am. J. Phys.*, *51*, 118–126.

Master, M. J., M. A. Uman, Y. T. Lin, and R. B. Standler (1981), Calculations of lightning return stroke electric and magnetic fields above ground, *J. Geophys. Res.*, *86*, 12,127–12,132.

McHarg, M. G., H. C. Stenbaek-Nielsen, T. Kanmae, and R. K. Haaland (2010), Streamer tip splitting in sprites, *J. Geophys. Res.*, *115*, A00E53, doi:10.1029/2009JA014850.

Pasko, V. P., U. S. Inan, T. F. Bell, and Y. N. Taranenko (1997), Sprites produced by quasi-electrostatic heating and ionization in the lower ionosphere, *J. Geophys. Res.*, *102*, 4529–4561.

Pawar, S. D., P. Murugavel, and D. M. Lal (2009), Effect of relative humidity and sea level pressure on electrical conductivity of air over Indian Ocean, *J. Geophys. Res.*, *114*, D02205, doi:10.1029/2007JD009716.

Rakov, V. A., and M. A. Uman (2003), *Lightning Physics and Effects*, Cambridge Univ. Press, Cambridge, U. K.

Roussel-Dupré, R., and A. V. Gurevich (1996), On runaway breakdown and upward propagating discharges, *J. Geophys. Res.*, *101*, 2297–2312.

Sentman, D. D., E. M. Wescott, D. L. Osborne, D. L. Hampton, and J. J. Heavner (1995), Preliminary results from the Sprites94 aircraft campaign: 1. Red sprites, *Geophys. Res. Lett.*, *22*, 1205–1208.

Stanley, M., M. Brook, P. Krehbiel, and S. A. Cummer (2000), Detection of daytime sprites via a unique sprite ELF signature, *Geophys. Res. Lett.*, *27*(6), 871–874, doi:10.1029/1999GL010769.

Uman, M. A. (1987), *The Lightning Discharge*, 377 pp., Academic, San Diego, Calif.

Uman, M. A., and D. K. McLain (1969), Magnetic field of the lightning return stroke, *J. Geophys. Res.*, *74*, 6899–6910.

Uman, M. A., D. K. McLain, and E. P. Krider (1975), The electromagnetic radiation from a finite antenna, *Am. J. Phys.*, *43*, 33–38.

U.S. Air Force (1960), *Handbook of Geophysics*, MacMillan, New York.